Detection and analysis of tau–neutrino interactions in DONUT emulsion target

K. Kodama[a], N. Saoulidou[b], G. Tzanakos[b], B. Baller[c], B. Lundberg[c],
R. Rameika[c], J.S. Song[d], C.S. Yoon[d], S.H. Chung[d], S. Aoki[e], T. Hara[e],
C. Erickson[f], K. Heller[f], R. Schwienhorst[f], J. Sielaff[f], J. Trammell[f], K. Hoshino[g],
H. Jiko[g], J. Kawada[g], T. Kawai[g], M. Komatsu[g], H. Matsuoka[g], M. Miyanishi[g],
M. Nakamura[a],*, T. Nakano[g], K. Narita[g], K. Niwa[g], N. Nonaka[g], K. Okada[g],
O. Sato[g], T. Toshito[g], V. Paolone[h], T. Kafka[i]

[a] *Aichi University of Education, Kariya, Japan*
[b] *University of Athens, Greece*
[c] *Fermilab, Batavia, IL 60510, USA*
[d] *Gyeongsang University, Chinju, South Korea*
[e] *Kobe University, Kobe, Japan*
[f] *University of Minnesota, MN, USA*
[g] *Department of Physics, F-Lab, Nagoya University, Furo-cho, Chikusa, Nagoya 464-8602, Japan*
[h] *University of Pittsburgh, Pittsburgh, PA 15260, USA*
[i] *Tufts University, Medford, MA 02155, USA*

Abstract

The DONUT experiment used an emulsion/counter-hybrid-detector, which succeeded in detecting tau–neutrino charged-current interactions. A new method of emulsion analysis, NETSCAN, was used to locate neutrino events and detect tau decays. It is based on a fully automated emulsion readout system (Ultra Track Selector) developed at Nagoya University.

The achieved plate-to-plate alignment accuracy of ~ 0.2 μm over an area of 2.6 mm $\times$ 2.6 mm permitted an efficient and systematic tau decay search using emulsion data. Moreover, this accuracy allowed measurement of particle momenta by multiple Coulomb scattering, and contributed to the efficient background rejection for the v_τ candidates. This paper describes details of our emulsion analysis methods.

*Corresponding author. Tel.: +81-52-789-2443; fax: +81-52-789-2864.
E-mail addresses: nakamura@flab.phys.nagoya-u.ac.jp (M. Nakamura).

1. Introduction

The first observation of tau–neutrino charged-current interactions was made by our experiment [1]. Nuclear emulsion was used as a three-dimensional tracking device with sub-micron accuracy, which enabled the detection of a short-lived τ particle in a v_τ charged-current interaction.

The analysis of nuclear emulsion used to be a time-consuming effort relying on human scanners until the invention of a semi-automated emulsion scanning system, first used in FNAL experiment E531 [2]. Though successful results were obtained using this system [3,4], the analysis speed was limited because it still required some human intervention. A prototype of the fully automated system, called Track Selector (TS), appeared in 1984 [5,6], and was first used in the analysis of the CHORUS experiment [7].

In CHORUS, the analysis was performed by using the first generation TS system in conjunction with predictions from an electronic vertex detector. All the tracks reconstructed in the vertex detector were located on the downstream face of the target and followed to the interaction or decay vertices.

In DONUT, a much faster scanning system and a new offline analysis procedure (called NET-SCAN) was required due to a greater number of background tracks that were recorded during the run. Also, the track reconstruction by the vertex detector was often poor because of electromagnetic showers in the thicker emulsion targets.

Following a description of the DONUT emulsion/fiber hybrid target, details of the analysis are discussed, emphasizing methods developed for this experiment.

2. DONUT emulsion-SFT hybrid target

2.1. Structure

The DONUT hybrid target has four emulsion stations interleaved with Scintillating Fiber Tracking (SFT) stations. A schematic view of the DONUT hybrid target is shown in Fig. 1. The thickness of each emulsion target is 7 cm corre-

Fig. 1. A schematic view of the DONUT emulsion-SFT hybrid target.
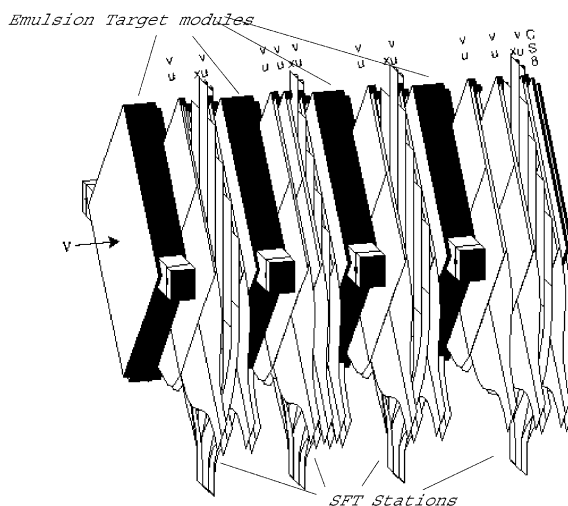
sponding to 2–3 radiation lengths depending on the target type as described below. The SFT was used to find the emulsion station in which a neutrino interaction occurred and to predict the vertex position in the emulsion target by detecting emerging tracks from the interaction.

2.2. Emulsion target

There were three distinct emulsion target designs that were exposed in the experiment. All were repeated structures of emulsion sheets stacked perpendicular to the neutrino beam direction. Fig. 2 shows the stacking pattern for the three designs. Each design was built from a type of emulsion sheet distinguished by the thickness of the emulsion coating and the supporting plastic or base layer. The three types of emulsion plates were called ECC200, ECC800 and Bulk.

The plate used in ECC200 had a thin plastic base of 200 μm with a 100 μm coating of emulsion on both sides. ECC800 had 100 μm emulsion coatings on an 800 μm plastic base. The Bulk plates had thick emulsion layers of 350 μm on both sides of a 90 μm plastic base. All emulsion plates were 50 cm × 50 cm (perpendicular to the beam). The deviation of the emulsion thickness
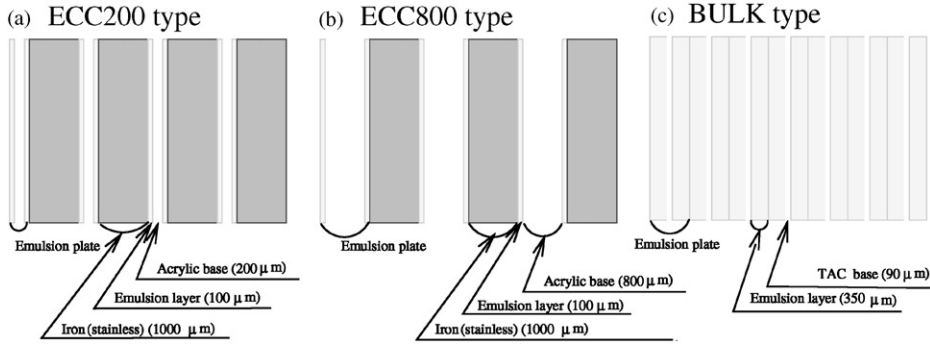
Fig. 2. Structure of the emulsion target with the three basic configurations: (a) ECC200, (b) ECC800 and (c) Bulk. Exposed emulsion modules were combinations of these structures.

was measured to be about 4 μm in one emulsion plate. For a limited area like 1 mm × 1 mm, which is the typical size for event analysis, the flatness was normally within 1 μm.

In the two structures named Emulsion Cloud Chamber (ECC), stainless-steel plates 1 mm thick were interleaved with the emulsion plates in the target assembly. (The thickness deviation of the stainless-steel plates were measured to be 5 μm. It was much better than this value in the case of within one plate.) The neutrino interactions predominantly occurred in the steel. The emulsion plates acted effectively as a three-dimensional tracking device. In the bulk type, no steel plates were incorporated, and the emulsion layers acted as the neutrino target as in the case of the CHORUS emulsion target.

The emulsion sheets were stacked into sealed target boxes as shown in Fig. 3. The plates were kept compressed and fixed under a pressure of ∼0.2 atm created by evacuation of air in the box. Each target box was made by screwing and gluing two 1 cm thick aluminum honeycomb plates at the upstream and downstream ends on a 7 cm thick aluminum frame. In addition to forming the structure of the target box, the honeycomb plates were designed to hold special emulsion sheets called Changeable Sheets (CS). The CS was a special emulsion sheet used to connect SFT tracks to the emulsion target. The CS were replaced frequently during the run to keep the accumulated track density low compared to the main emulsion target. A grid of collimated X-ray sources on the
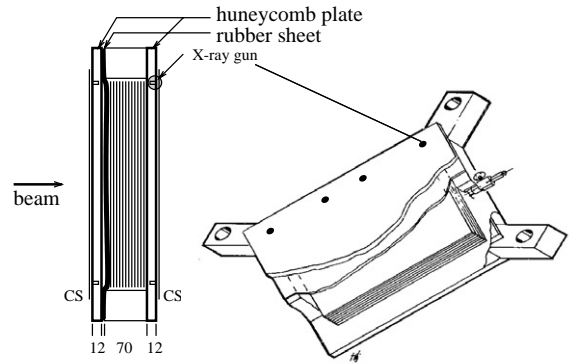

Fig. 3. A schematic view of an emulsion target module. A cross-sectional view is shown to the left.

honeycomb plate formed marks on each exposed CS for spatial calibration.

2.3. Scintillating fiber tracker

There were four stations of the SFT as shown in Fig. 1. However, in construction, the SFT was composed of only two independent modules. Thus, there were two stations per module as shown in Fig. 4. The upstream station of each module (indicated as SFT1 in the figure) consists of two u/v doublet planes (the fibers aligned $\pm45°$ with respect to vertical) and one x plane (the fibers aligned vertically) and the downstream station (SFT2 in the figure) has three u/v doublet planes and one x plane as shown in the figure. There was a total of 44 SFT planes in all stations. All planes
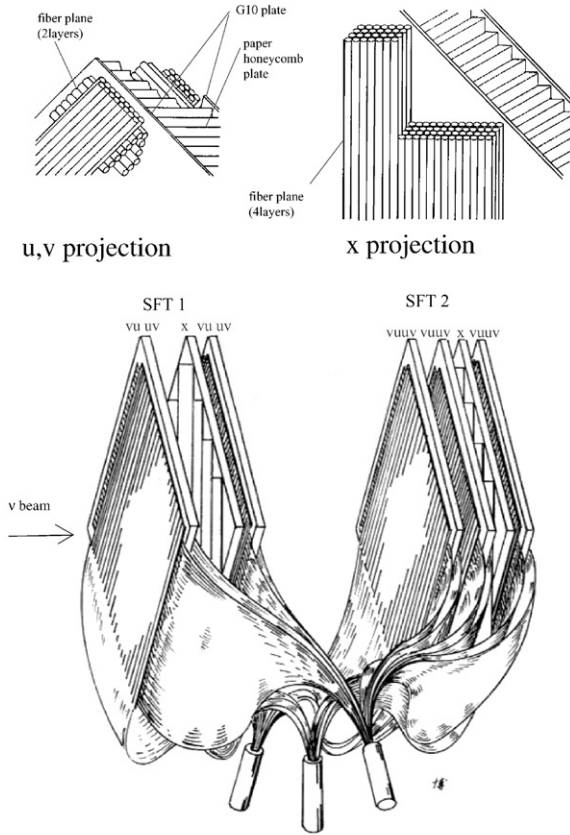
u,v projection   x projection

Fig. 4. A schematic view of one SFT module.

in each station were mechanically fixed together with an accuracy of ~ 50 μm.

For each u/v doublet plane, two-layered scintillating fiber sheets were glued on both sides of a honeycomb plate (11 mm thick). Each x plane consisted of four layers of fibers. The glued positions of the fiber sheets on the plane were measured by an x–y stage with the accuracy of 10 μm. The 500 μm diameter fiber was made from SCSF78 produced by Kuraray Co. The dopant density was tuned to maximize the light yield at the farthest position (~ 120 cm) from the readout ends. In addition, the far end of the fiber was aluminized. The light yield of the two-layered fiber sheet was about 7 photo-electrons when a minimum-ionizing particle passed through the farthest position. The fiber sheets were produced by the same machines installed at Nagoya which were

used for the production of CHORUS fiber trackers [8].

The ends of the fiber sheets were stacked into paddles in contact with the input fiber-optic windows of six Image Intensifier Tubes produced by Hamamatsu Photonics K.K. The images were read out by CCD cameras and digitized for the triggered events. The hit positions on the CCD images were decoded to fiber coordinates by using maps calibrated by a set of fiducial fibers. The fiducial fibers were flashed for each data run and the positions were monitored for any systematic shifts.

2.4. Alignment between the emulsion target and the SFT

The emulsion modules and the SFT stations were installed on a mechanical support composed of two I-beams holding precision mounting hardware. The design accuracy of the mechanical support was 50 μm. The alignment between the emulsion targets and the SFT stations were checked and fine-tuned by using special cosmic ray exposures. For this exposure, seven new CS plates were installed in the CS holders. In the recorded events, tracks with angle smaller than 400 mrad were selected and scanned on the CS plates. The cosmic-ray tracks were reconstructed in the SFT station just upstream of each CS plate, and projected to the CS. The distribution of the residuals between the projections and the found tracks are shown in Fig. 5. The rms of the distribution is consistent with measurement errors. The mean of the distributions indicate the shift from design within the mechanical accuracy, shown in Fig. 6.

3. Beam exposure

A "prompt" neutrino beam was created by interacting 800 GeV/c protons in 1 m long tungsten beam dump. The neutrino beam that was created had the following approximate composition: 60% ν_μ, 35% ν_e, and 5% ν_τ, with equal numbers of anti-neutrinos and neutrinos. The emulsion target was 36 m downstream of the

beam dump. In addition to the emulsion targets and SFT, the DONUT detectors consisted of a magnetic spectrometer, electromagnetic calorimeter and muon identifier. The average neutrino energy was 53 GeV. Details of the prompt neutrino beam and the DONUT detector other than the emulsion targets are described in another paper [9].

The physics data was taken from April to September 1997. The effective total number of protons-on-target was 3.5×10^{17}. Because of high backgrounds from muons and neutrons from the dump, and γ rays from muon showers, all the emulsion modules were replaced once to insure the recorded backgrounds were at a tolerable level.

In Table 1, summary of the exposure for each module is listed. The calculated number of neutrino events in our modules are ~ 1100 events. Reconstruction of the triggered events using the counter-information yielded 840 events [9].

After exposure, fiducial marks were printed on all of the emulsion plates which were then developed. A coarse coordinate alignment with
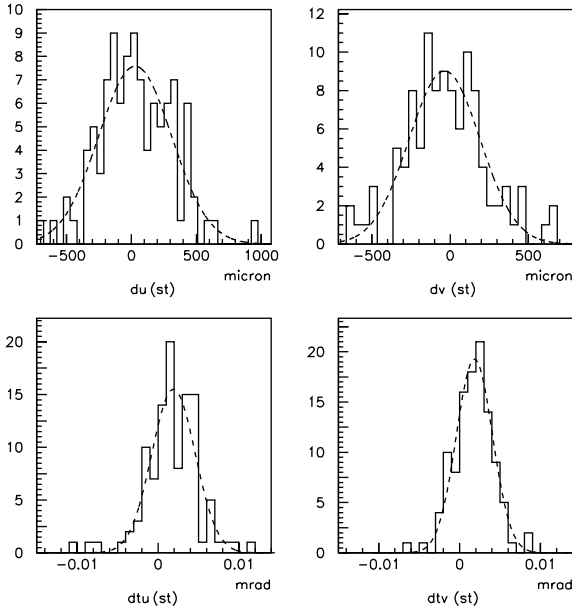

Fig. 5. Residual distributions of position (top figures) and angle (bottom figures) between the predictions and the found tracks for cosmic ray calibration. The rms of the distributions are 280 μm for u, 230 μm for v, 2.7 mrad for θ_u and 2.2 mrad for θ_v. The theoretical resolution is 220 μm for u/v and 2.2 mrad for θ_{proj}.

Table 1
Information about the exposed emulsion modules

Module	Composition	Mass (kg)	n_{POT} $\times 10^{16}$	Expected v events
mod 1	ECC200 × 47	104	20.1	236
mod 2	ECC800 × 19 + Bulk × 38	70	25.8	202
mod 3	ECC200 × 47	104	9.8	115
mod 4	ECC200 × 2 + ECC800 × 7 +Bulk × 47	70	14.7	115
mod 5	ECC800 × 21 + Bulk × 30	71	15.5	124
mod 7	ECC800 × 20 + Bulk × 32	70	25.8	203
mod 8	Bulk × 87	60	15.5	105
Total				1100

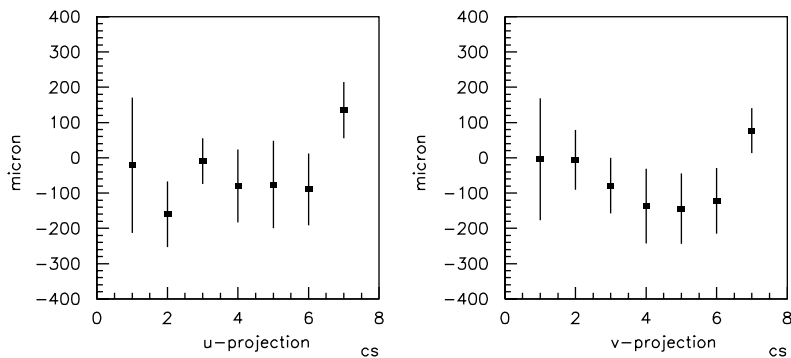Here n_{POT} is the number of 800 GeV protons on target.

Fig. 6. Observed shift between the emulsion and SFT coordinates.

an accuracy of 10 μm was obtained by using these marks.

4. Neutrino event location

4.1. Vertex prediction and emulsion read-out

Using the information from the SFT, the reconstructed events were divided into three categories. Category (1): less than three tracks are emitted from the vertex (Fig. 7). Category (2): at least three tracks were emitted from the vertex and the predicted vertex position was less than 10 mm transverse to the beam (Fig. 8). Category (3): the vertex position accuracy was greater than

10 mm transverse to the beam (Fig. 9). The number of events in each category was 138, 533 and 83, respectively.

Finding a vertex for category (1) events was difficult because of the high density background tracks that were accumulated during the run. Further analysis was suspended. Category (3) events were also deferred because greater scanning capability will be required for the analysis.

For category (2) events, a prediction was made for the vertex position for each event, with the calculated errors. This prediction determined the location and size of the scanning volume in an emulsion target.

Emulsion plates containing the predicted volume were read-out by the present-generation
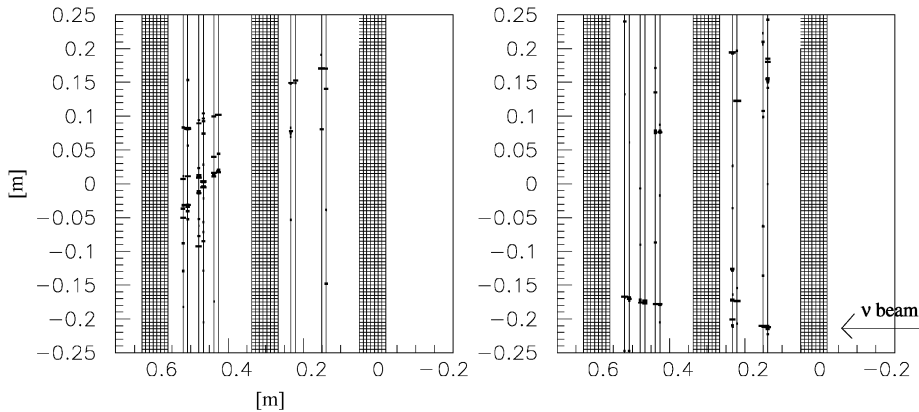

Fig. 7. A recorded neutrino event of category (1); Left: U projection; right: V projection. Dots are the hits in each SFT plane.
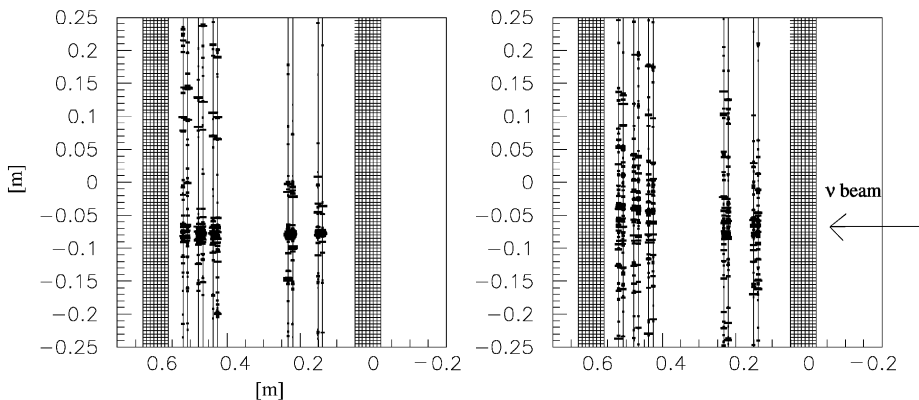

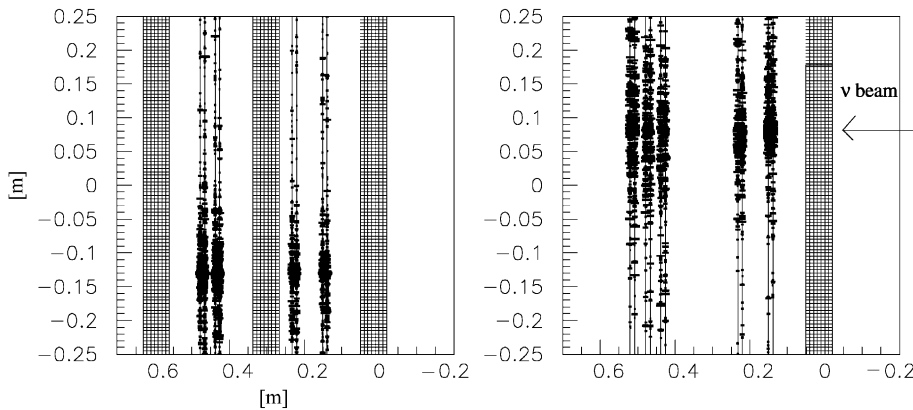Fig. 8. A recorded neutrino event of category (2).

Fig. 9. A recorded neutrino event of category (3). Note that each target station has material corresponding to 2–3 radiation lengths.

automatic scanning system, the Ultra Track Selector (UTS). The typical scanning volume was 5 mm × 5 mm transverse to the beam and ~1.5 cm along the beam. For the ECC200 modules, typically 12 plates were read-out. For each of these plates, both emulsion layers were digitized. However, for Bulk plates, only ~100 μm of the 350 μm emulsion layer in the upstream side was read-out.

The UTS system is composed of a microscope installed on a computer controlled x–y–z stage, a CCD TV camera for image read-out, and a dedicated hardware processor to handle with the digitized tomographic images. Sixteen digitized images were taken by changing the focal position within an emulsion layer. Aligned grains across an emulsion layer were recognized as a track, which had at least 10 hits in these 16 digitized images. The output data from the UTS was the position, the angle and the pulse height of the recognized tracks (called "micro-tracks"). Pulse height is defined as the number of hits in the 16 images. Track recognition is described in detail in Refs. [5,6]. For the UTS, the track angle was limited to be within 400 mrad, perpendicular to the emulsion plate.

The read-out speed of the UTS corresponded to ~1 cm²/h. For one plate (5 mm × 5 mm in area), ~15 min was required for the read-out. A single event needed about 6 h for digitization, including plate changing.
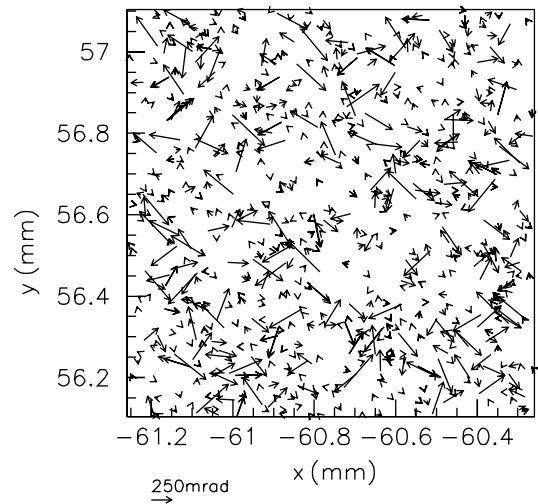
Fig. 10. A sample of the recognized tracks (micro-tracks) in one emulsion layer. The beginning of the arrow indicates the position of the micro-track and the length is proportional to the measured angle.

Fig. 10 shows an example of the recognized micro-tracks. There are about 800 micro-tracks in a 1 mm × 1 mm area. The origin of the micro-tracks includes not only the high-energy muons or hadrons, which are used for event location and calibration, but also a background of low-energy tracks arising from Compton scattering of γ rays that were recognized as tracks by the UTS.

4.2. Track reconstruction and alignment

To reconstruct complete tracks in the event, a large number of background tracks recorded in the read-out volume were also reconstructed. These tracks were used to precisely align the emulsion layers.

The complete tracks were built layer by layer. Each track recognized in an emulsion layer was examined to see if it had a connectable micro-track in the adjacent emulsion layers. As shown in Fig. 11, the angle differences ($\Delta\theta$) between the micro-tracks and the connected-tracks (θ) and the position displacements (Δr) between the extrapolated positions were the parameters of the layer by layer alignment.

The essential tuning parameters were the distance between the emulsion layers (L), the relative shifts in transverse direction (x, y) and the shrinkage of the emulsion layers. The measured $\Delta\theta$ was also affected by emulsion distortions. Because of these errors and the high track density, a micro-track can have multiple connectable micro-tracks within the spatial and angular tolerance, which were basically determined by the measured rms of the distributions of $\Delta\theta$ and Δr.
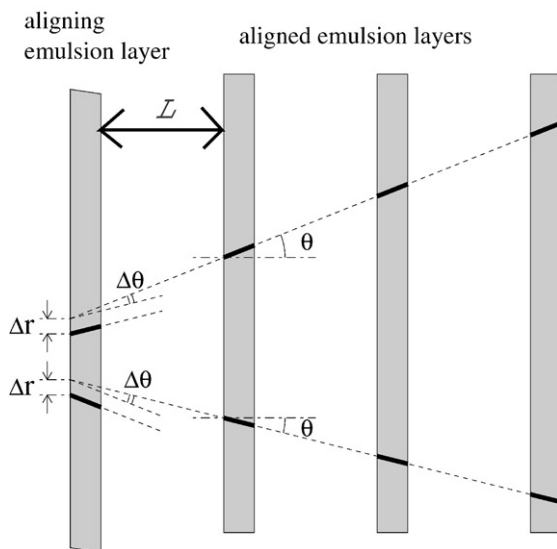
For all tolerable combinations, the angular differences and position displacements were calculated. The distribution of these parameters for the wrong combinations should be flat, while the distribution of correct combinations was peaked. Using the correct combinations from the peak, the position displacements and angular shifts were calibrated. From the correlation between Δr and θ, the distances between layers were calibrated, and from the correlation of $\Delta\theta$ and θ, shrinkage parameters of the emulsion layers were calibrated.

After these calibrations, the spatial and angular tolerances were reduced and micro-track connection was retried using the smaller tolerances. Repeating these corrections, the rms of $\Delta\theta$ and Δr are minimized and the number of correct combinations were maximized.

Fig. 12 shows the distribution of the angle residuals ($\Delta\theta_x$ and $\Delta\theta_y$) and the position residuals (Δx and Δy) after the correction. After the corrections, a track was judged to be connected when $\Delta\theta \leqslant 3 \times \sigma_\theta + 0.05 \times \sqrt{\tan^2\theta_x + \tan^2\theta_y}$ and $\Delta r \leqslant 3 \times \sigma_r + 10\ \mu m \times \sqrt{\tan^2\theta_x + \tan^2\theta_y}$, where σ_θ and σ_r are the rms values of the residual distributions shown in Fig. 12. These criteria filtered out the tracks with low momenta due to multiple scattering in the steel plates.

Following the plate-by-plate connections, an additional "fine" alignment was tried by selecting relatively high momentum tracks, which were fully connected through the scanned volume. High momentum tracks were selected by comparing the angles in the upstream and the downstream of the scanning volume. The angles were reconstructed by using the first three or the last three micro-tracks at the upstream end or downstream end, respectively. The required angle difference of less than 2.4 mrad for a track traversing 10 mm of iron was equivalent to requiring a momentum greater than 9 GeV/c. After fine-tuning of the rotation and shrinkage of the plates, the measured position residuals were distributed as shown in Fig. 13. The position residuals for each projection, i.e. position resolution of the plate, was $\sigma_{x,y} \sim 0.2\ \mu m$.

The position resolution of an emulsion plate was defined as $\sqrt{\sigma_x^2 + \sigma_y^2}$. Fig. 14 shows the distribution

Fig. 11. Parameter definitions used for the track connection and the emulsion layer alignment.
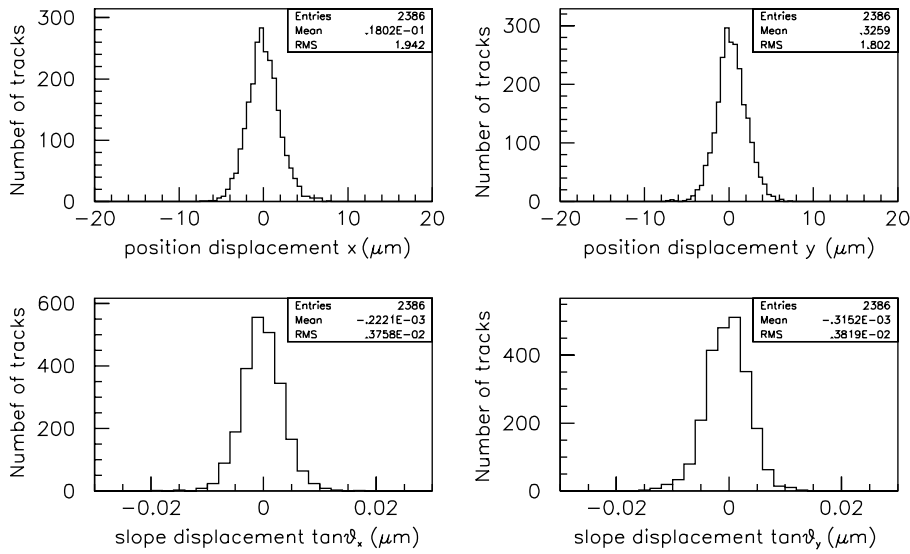
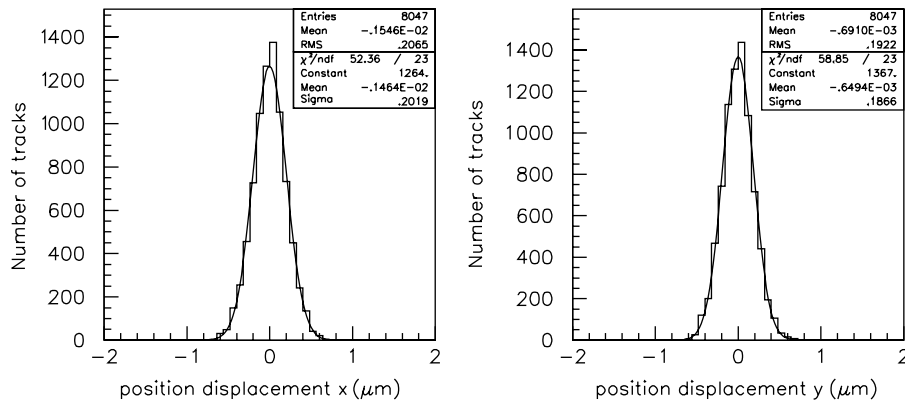Fig. 12. Residual distributions of the position and the angle after the plate-by-plate connection.

Fig. 13. Residual distribution for high momentum tracks after the plate-by-plate correction.

of the measured resolution of emulsion plates for ECC200, ECC800 and Bulk type. The distributions have a peak at 0.3 μm for the ECC types, and peak at 0.4 μm for Bulk plates. These distributions have tails beyond 1 μm. The origin of this degradation was investigated by using a sample of 79 scanned areas that had a resolution greater than 1 μm in any projection. It was found that all 79 samples suffer from a slipping of emulsion plates relative to each other during the exposure.

The slipping was discovered by observing multiple peaks in the data for the plate-by-plate alignment. As shown in Fig. 15, one peak was observed in the normal case, but in the case of slipping the distribution has several peaks, which indicate that the relative position between plates changed during the exposure. The slipping was probably due to temperature and pressure variations during the exposure. At present, these plates have been rejected from the fiducial volume of the vertex location described later.

As noted above, the tracking resolution in Bulk plates was worse than the ECC plates. The origin of this effect was found to be local distortions in the emulsion layers. To understand this effect, a set of ECC and Bulk plates with typical resolution
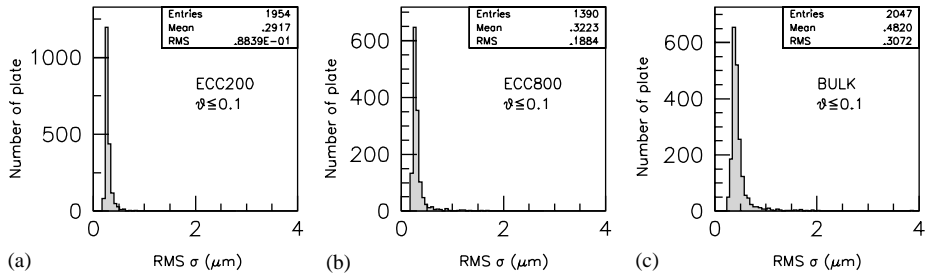
Fig. 14. Position rms distribution of (a) ECC200, (b) ECC800, and (c) Bulk plates.
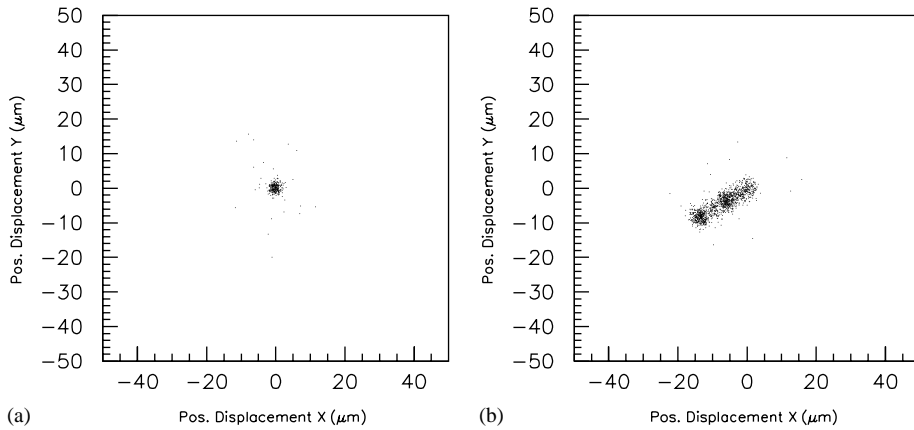

Fig. 15. Residual distribution for high momentum tracks after the plate-by-plate correction in the case of (a) no slipping and (b) slipping.
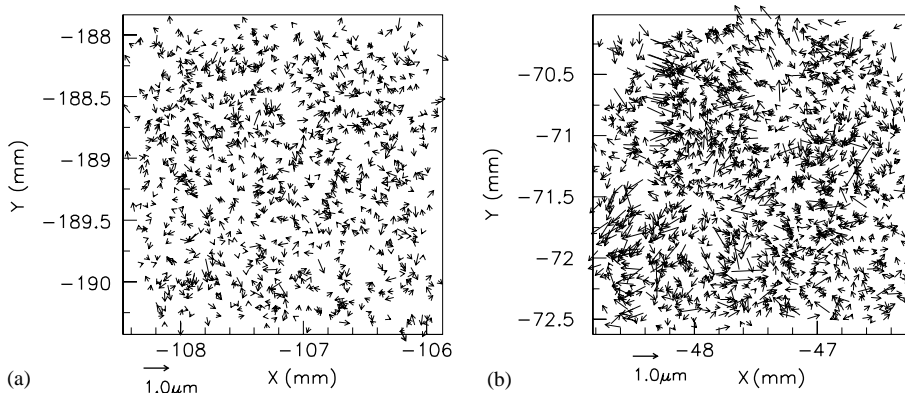

Fig. 16. Observed distortions in the case of (a) ECC200 and (b) Bulk plate.

were selected. The distortion was measured from the angular difference between the recognized micro-tracks and the tracks connected across the base. As shown in Fig. 16, the size of the distortion

was larger for Bulk plates. The origin of this distortion was the accumulated stress during plate production, when swelling and then shrinking of the emulsion layer occurs. The Bulk plate, which
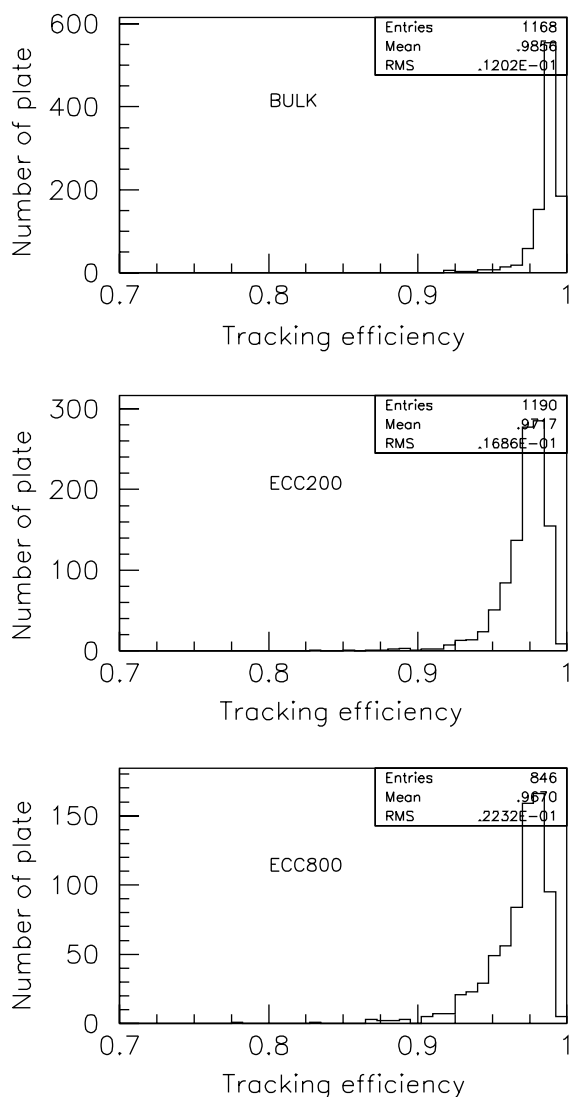
Fig. 17. Track detection efficiency of the emulsion plates. Inefficiency was mainly due to degraded emulsion quality such as dirty surfaces, and large distortions.

had much thicker emulsion layers than ECC plates, had correspondingly larger distortions.

The track detection efficiency for each emulsion plate was computed by checking for the existence of hits in all the emulsion layers along penetrating, reconstructed tracks. Fig. 17 shows the distribution of the measured efficiency for each emulsion plate. The efficiency was lower for ECC plates compared to Bulk plates.

The origin of the inefficiency was investigated by checking the quality of the emulsion plates that had an efficiency less than 90%. The number of low efficiency areas in the data were 10 out of 2047 for Bulk and 26 out of 1910 for ECC. In the set of 10 Bulk plates, eight had dirty emulsion surfaces or large local distortions. For the 26 ECC data sets, only eight had a dirty emulsion surface or large distortions. In the remaining 18 sets, 15 had a pulse height below the threshold set for track recognition. This low pulse height was due to anomalously thin emulsion layers or low grain densities. Unfortunately, the quality of the hand-made emulsion plates was not consistent. The overall efficiency for detecting micro-tracks was measured to be greater than 97%.

4.3. Vertex location

4.3.1. Procedure
In order to select the tracks from a neutrino interaction vertex and reject the background muons in the scanning volume, the following criteria were applied sequentially: (1) Tracks must be started within the volume and have no connectable micro-tracks in the two adjacent upstream emulsion layers. This requirement rejects the penetrating tracks efficiently. (2) Tracks must be constructed from at least three micro-tracks. (3) The χ^2/naf ($naf = 8$) defined by the first three micro-tracks must be smaller than 2.5. Cuts (2) and (3) greatly reduced tracks of low momenta.

Fig. 18(a) illustrates the effect of the above cuts on the emulsion data after alignment. A large number of tracks were typically reconstructed in the scanning volume. The tracks are mostly penetrating muons originating from the dump. The muon track density depends somewhat on the target position, and in the figure it is about 12,000 tracks per 5 mm × 5 mm. The tracks from the neutrino interaction were isolated in this sea of background tracks. The next plot in the sequence, Fig. 18(b), shows the same data after cuts (2) and (3) with 264 tracks remaining.

Next, (4) the remaining tracks were tested for vertex topology. At least three tracks were required to be associated such that all impact
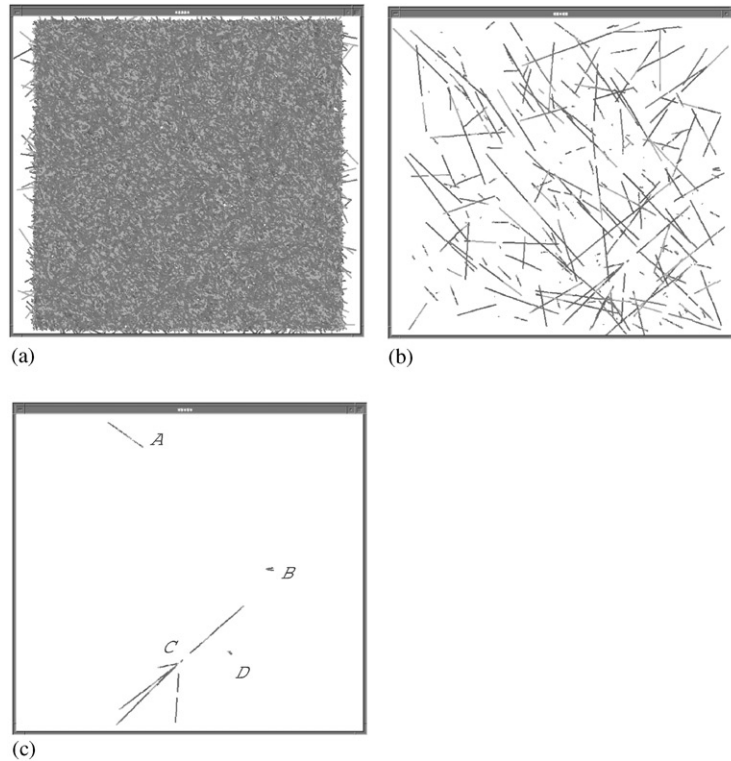
Fig. 18. Vertex location sequence by the NETSCAN in the case of a event (Run 3118 Event 11989): (a) after alignment, (b) after the rejection of penetrating tracks, and (c) after the vertex requirement.

parameters at the best vertex position were less than 4 μm.

After the vertex requirements were imposed, only a few vertex candidates remained. To confirm a vertex candidate, (i) the emulsion plates near the vertex point were investigated using a manually controlled microscope and (ii) the emulsion track information was compared with the hits in the SFT.

By the manual check (i), candidates A and B were identified as fake vertexes. In the case of A, two tracks created the vertex. But these two tracks have penetrated to the upstream. This was caused by the inefficiency of the UTS and misconnections of the offline processes. In the case of B, two tracks, which created the vertex, were low momentum tracks and were not connected to upstream because of large multiple scattering. Candidates C and D were the real vertexes. D

has two tracks with small relative angle, which is consistent with an electron pair creation. C has seven tracks as shown in Fig. 18(c). After applying the vertex constraint (ii), candidate C was selected.

4.3.2. Efficiency

By December 2001, vertex location was attempted for category (2), 533 events and 337 events, were confirmed as being located.

The reason of the failure of the vertex location was investigated. At first the data set quality was checked. As described above, the data quality is corresponding to the plate quality contained in the data sample. Dependences of the vertex location efficiency on the position resolution of the plate and on the track detection efficiency of the plate were checked.

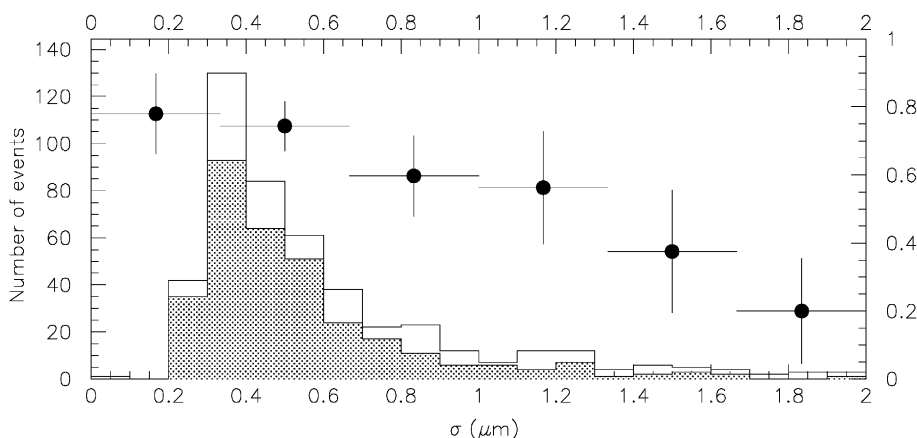Figs. 19 and 20 show the vertex location efficiency dependence on the resolution of the

Fig. 19. Dependence of the vertex location efficiency on the position resolution of the worst quality plate among the data set.
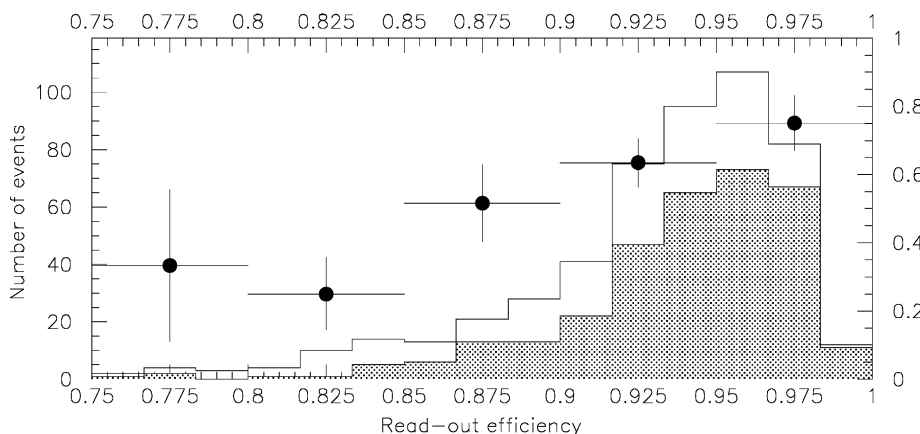

Fig. 20. Dependence of the vertex location efficiency on the track detection efficiency of the worst quality plate among the data set.

worst quality plate contained in the data set and on the track detection efficiency of the worst quality plate. The event location efficiency gradually decreases when the plate quality becomes worse.

Table 2 shows the categorization of the event quality and Table 3 shows the vertex location efficiency of each category. For the good quality samples, the location efficiency reach to $\sim 76\%$.

There are small differences between ECC200, ECC800 and Bulk, even in good quality samples. The location efficiency is 69%, 73% and 84%, respectively. For these good quality samples, the location efficiency dependence on the depth (radiation lengths) was checked. Fig. 21 shows the result for each target type. Generally, it was

Table 2
Quality of the NETSCAN data

Plate type	Number of events	Good quality $\sigma^{worst} \leqslant 1.0$ μm and $\varepsilon^{worst} \geqslant 0.9$	Bad quality $\sigma^{worst} \geqslant 1.0$ μm or $\varepsilon^{worst} < 0.9$
ECC200	152	115	37
ECC800	174	91	83
Bulk	208	132	76
Total	533	338	195

more difficult to locate events in the upstream part of the emulsion target, which is readily seen for the ECC200 type. Clearly, one reason why the upstream location efficiency was poor was the reduced accuracy of the vertex prediction.

Table 3
Dependence of the vertex location efficiency on the data set quality

Plate type	Good quality		Bad quality	
	Tried event	Found event (Location efficiency)	Tried event	Found event (Location efficiency)
ECC200	115	79(69%)	38	21(55%)
ECC800	91	67(73%)	84	21(25%)
Bulk	132	111(84%)	80	38(48%)
Total	338	257(76%)	195	80(41%)
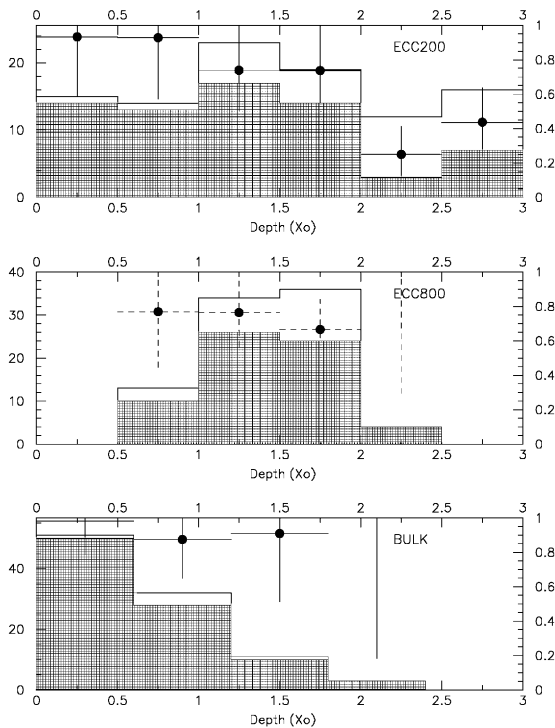
Fig. 21. Dependence of the vertex location efficiency on the vertex depth from the SFT (neutrinos come from the right). Solid-line histogram: number of predictions; filled histogram: number of found events. The open circles indicate the ratio of number of found events to the predicted number (scale on the right).

Therefore, to increase the efficiency, the scanning volume could be enlarged, but this would require a more powerful scanning system. The next-generation emulsion read-out system, called "S-UTS", is under development in order to meet such increased demands [10].

5. Decay search

5.1. Decay search volume

For the located events, a smaller volume around the located vertex was digitized again in order to optimize scanning acceptance and precision for detecting tau decays. The scanning volume was 2.6 mm × 2.6 mm and the length was nominally 1.2 cm. The same track reconstruction procedure used for the vertex location was also applied for the new data, to confirm the vertex. When slipping plates were included in the volume, background muon tracks that have the same alignment parameters of the event-related tracks were selected and used for the precise alignment (aimed accuracy $<1\,\mu m$, which is corresponding to the error of the kink angle to be less than 1mrad, e.g. $1\,\mu m/(1000 + 300\,\mu m)$).

The tau decay search was divided into two categories by the topology, as shown in Fig. 22: (i) long-flight path decay search and (ii) short-flight path decay search. In the first case, both the parent and the daughter tracks were present in the emulsion data. In the second, only the daughter could be detected.

5.2. Topological decay search : long flight decay

A general search for decays of long lived tau leptons and charmed mesons began by trying to link tracks from the interaction vertex with all other tracks defined by the following criteria: (1) the tracks must start downstream of the vertex, (2) the tracks were composed of at least three
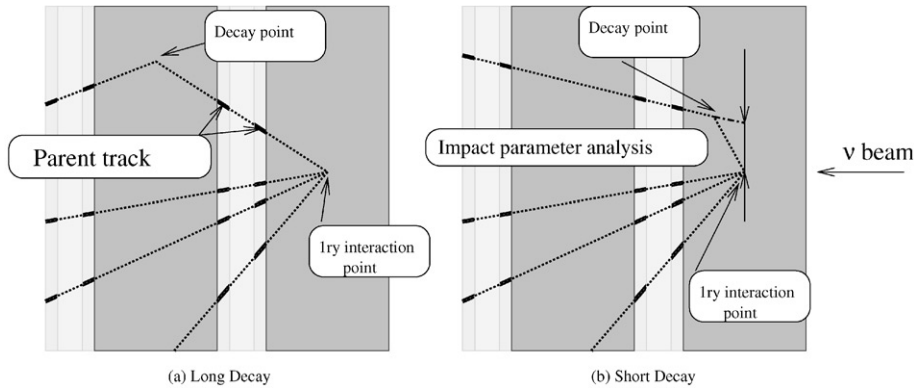
Fig. 22. Decay search topology was divided into two categories: (a) Long-flight decay search where the parent tau *and* the daughter can be observed, and (b) short-flight decay search where only the daughter particle can be detected by a non-zero impact parameter to the vertex.
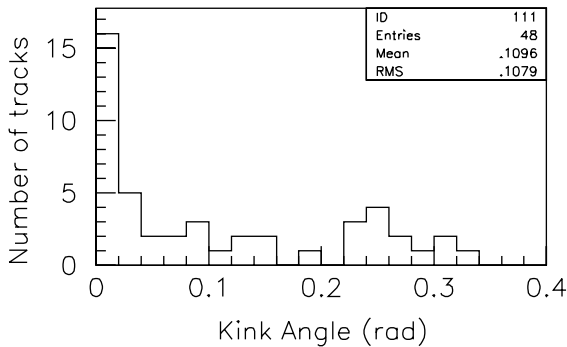

Fig. 23. Kink angle distribution of the detected long-flight-decay candidates.

micro-tracks, and (3) the fitted χ^2/naf of the first three micro-tracks should be smaller than 2.5 and (4) the distance of closest approach between the parent candidate and the daughter was smaller than 5 μm.

With these cuts, 37 events (48 tracks) were selected. Fig. 23 shows the angle distribution between the parent track and the daughter.

The above selection may have failed, however, for decays with an angle between the parent and daughter of less than 15 mrad. For these cases, there was a possibility that the parent and the daughter coalesced into one track. This possibility was checked for all of the tracks from the vertex using the following procedure.

Each track from the vertex, which was composed of micro-tracks, was divided into two tracks, refitted and the angle difference between them was computed. These steps were then repeated by changing the dividing point as shown in Fig. 24. When the angular difference was larger than 5 mrad, the case was investigated further. The detection efficiency has a dependence on the position where the decay occurs. The expected sensitivity to the kink angle is shown in Fig. 25, estimated using muons penetrating through 10 plates. The sensitivity was estimated at 1.7 mrad which is defined as $3 \times \sigma_{\mathrm{measured}}$, except for the edge layers (5–6 mrad).

The following additional cuts were applied to the 1549 tracks in 344 events found with small kink angles: (1) $\theta_{\mathrm{meas}} \geqslant 3 \times \sigma_{\mathrm{meas}}$; (2) the parent segment must contain at least three micro-tracks; (3) the daughter segment must have at least three micro-tracks; and (4) the impact parameter to the vertex of the daughter track is greater than 5 μm. After these cuts 117 tracks remained, with the distribution of their detected kink angle shown in Fig. 26.

The tau and charm physics long-decay sample had three additional requirements: (1) the topology was limited to one prong or three prongs decay; (2) the impact parameter of the daughter particle to the primary vertex was less than 500 μm; and (3) ($\theta_{\mathrm{kink}} = |\theta_{\mathrm{daughter}} - \theta_{\mathrm{parent}}| \geqslant (\theta_{\mathrm{parent}} - 0.1)/2$). Both (2) and (3) were incorporated to reduce the number of low-energy interactions, with a negligible effect on tau decay efficiency.
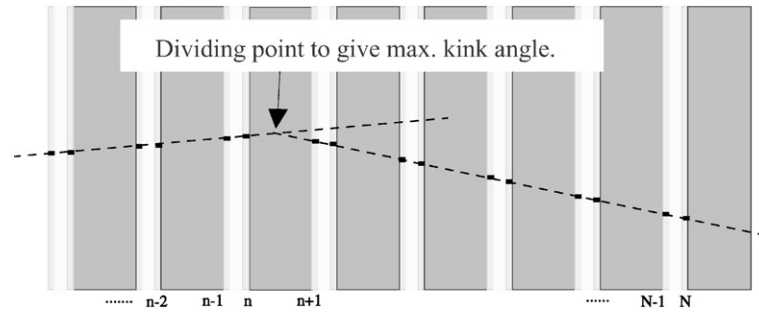
Fig. 24. Schematic view of the small angle kink detection. A track was split into two tracks at a reference point and the "kink angle" was determined for a series of reference points.
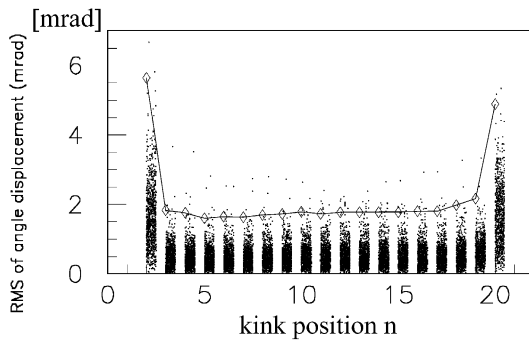

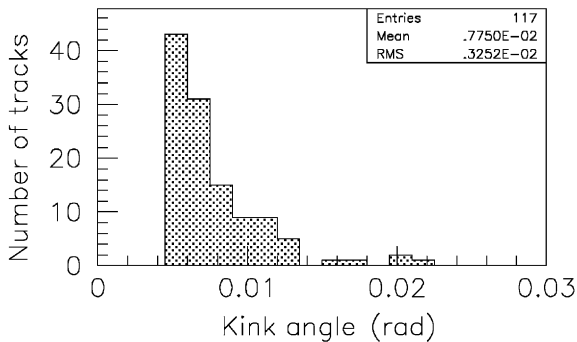Fig. 25. The sensitivity to small kinks in the study illustrated in Fig. 24.

Fig. 26. Detected kink angle distribution in the small kink search.

Sixty-four tracks in 60 events were selected from $48 + 117$ long-flight-decay candidates. The distribution of the detected angle is shown in Fig. 27.
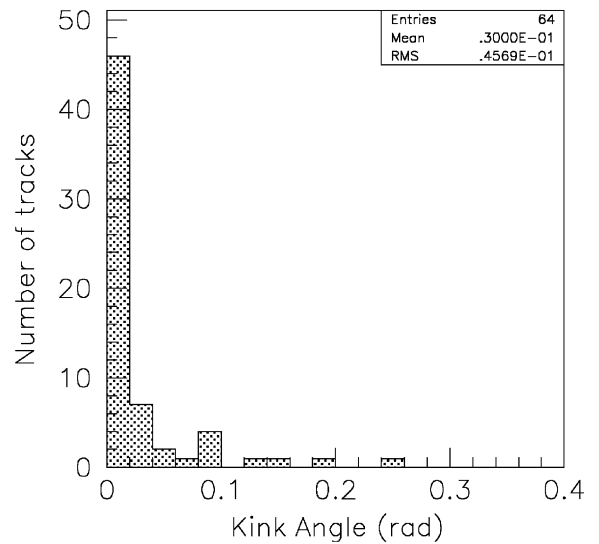

Fig. 27. Angle distribution between the parent track and the daughter long-flight decay search.

5.3. Topological decay search: short-flight decay

The short-flight decay search required the following criteria:

(1) The track started at one or two emulsion layers downstream from the located vertex.
(2) The impact parameter to the vertex is less than 200 μm.
(3) The track consists of at least three micro-tracks.

Pairs of tracks meeting these selection criteria are used to find daughter candidates. The closest approach between each pair of track was

calculated. The signal is pre-selected by applying a cut on the minimum distance, d_{min}, of the pair. The criteria are $d_{min} > 1.36 + 1.36 \times 10^{-3} \times \Delta z$ μm, $d_{min} > 1.52 + 1.02 \times 10^{-3} \times \Delta z$ μm and $d_{min} > 2.04 + 1.81 \times 10^{-3} \times \Delta z$ μm in the case of ECC200, ECC800 and Bulk, respectively. Here, Δz is the distance from the most upstream emulsion layer to the position where the closest approach occurs. This cut was calculated from the measurement error, which was obtained during the alignment. Seventy-eight events were selected for further investigation.

6. Decay analysis

Candidates selected by the above procedures may contain tau decays, charm decays, secondary interactions and scattering of low-energy particles. To resolve these hypotheses, the momentum of the daughter tracks was measured and transverse momentum of the daughter with respect to the parent line of flight, P_t, was computed. All tracks in the event (including the daughter) were then checked to see if any were consistent with being a lepton (muon or electron) using the spectrometer.

6.1. Momentum measurement by multiple Coulomb scattering measurement

Although DONUT had a magnetic spectrometer, the efficiency for unambiguously linking SFT tracks with drift chamber information was low because of electromagnetic shower development in the thick emulsion targets.

An alternative momentum estimate was made using Multiple Coulomb Scattering (MCS) in the emulsion data. The emulsion data was not significantly affected by confusion in tracking and, in principle, momentum estimates were available to all the tracks in an event. A schematic overview of the principle of the MCS method is shown in Fig. 28.

The root mean square of the position displacement in one projection (y) is expressed as $y_{rms} \equiv \sqrt{\langle y^2 \rangle} = \sqrt{\frac{2}{3}} \times k/p\beta \times \sqrt{t/X_0} \times t$, where k is the scattering constant, p and β is the momentum and the speed of the track, t is the thickness of the material and X_0 is the radiation length of the material. The expected value of y_{rms} is 4.0 μm in the case of 1 GeV/c particle and the ECC with 1 mm thick iron plate. This value can be compared with the extrapolation error from the base track (1.5 μm $\sim \sqrt{1 + ((L1+L2)/L1)^2 + (L2/L1)^2} \times$ resolution (~ 0.2 μm), where $L1$ is the length of the base line (200 μm) and $L2$ is the extrapolation length (1 mm) in the case of ECC200).

The y_{rms} has $t^{3/2}$ dependence from MCS, but the measurement error is independent of t. This dependence allowed the measurement of higher momentum particles by increasing t so that the displacement was observable. It should be noted that a good plate-by-plate alignment by NETS-CAN procedure was indispensable for this measurement.
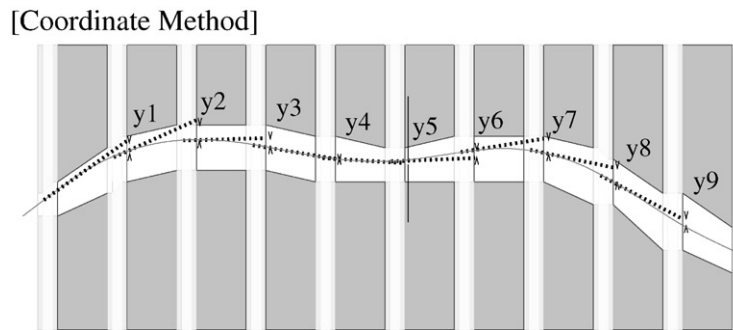
[Coordinate Method]

Fig. 28. Schematic figure of the momentum measurement by using the information of multiple Coulomb scattering. In the emulsion plates, the track path was measured with sub-micron accuracy.

The measured y_{rms}, y_{rms}^{meas}, was the addition of the y_{rms} from MCS and the measurement error ε_y: $y_{rms}^{meas} = \sqrt{y_{rms}^2 + \varepsilon_y^2}$. Since ε_y was measured in the alignment sequences as described in Section 4.2, one could estimate the y_{rms} confidently.

The distribution of y was described by a Gaussian distribution to a good approximation. The momentum of a track was extracted from the measured standard deviation, with the accuracy $\Delta y_{rms}/y_{rms}$ expressed as $1/\sqrt{2n}$, where n was the number of independent measurements. If 11 independent position measurements were used, giving 10 displacements, the error was 22%.

When slipping plate was included in the fiducial region, the track was divided into two tracks at the slipping plate. Momentum of each separated tracks were measured independently. The consistency between these measurements was checked and the measurements were combined if needed.

6.1.1. Check 1: test experiment

In order to check the validity of this method, an ECC-type stack with 29 bulk emulsion plates was exposed to a 4 GeV/c π^- beam at KEK. Fig. 29 shows the result of the dependence of the y_{rms}^{meas} on t. Here, y_{rms}^{meas} is the average of 384 tracks reconstructed in the chamber. The fit value is $y_{rms}(t) = \sqrt{(94.49(t/X_0)^{3/2} + 1.458^2)}$. This result is consistent with the measurement error. The scattering constant k was determined to be 16.02 MeV/c. The distribution of the MCS esti-

Fig. 30. Measured momentum distribution of 4 GeV/c π^- tracks.

Fig. 31. Correlation between the momentum measured by the MCS method and by the magnetic spectrometer. Solid circles indicate identified muons.
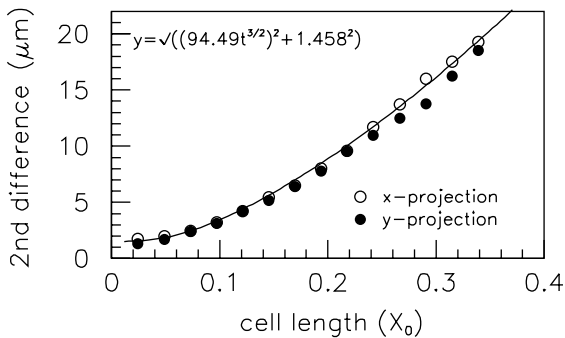

Fig. 29. Dependence of the position displacement on the cell length or thickness. Open circles: x projection, and solid circles; y projection. The fit is shown by the curve.
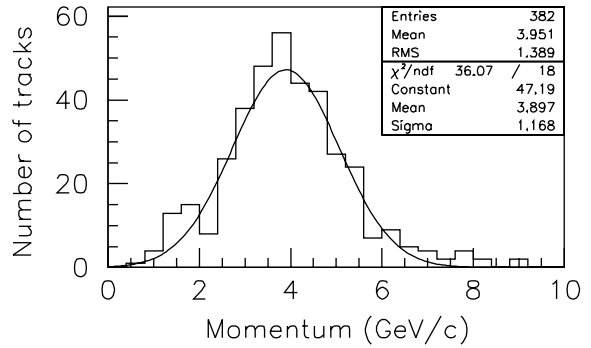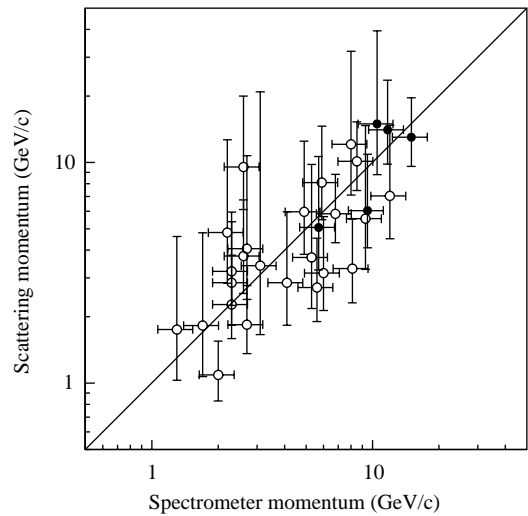
mated momentum for each track is shown in Fig. 30. The resolution of the momentum measurement was about 30%.

6.1.2. Check 2: spectrometer tracks

One can also check the MCS measurements with momenta estimated using the magnetic spectrometer. Care was used in selecting tracks that were well reconstructed and had no evidence of interaction in the target area. For these tracks, the momentum was estimated by the MCS method. The scatter plot between the MCS measured and
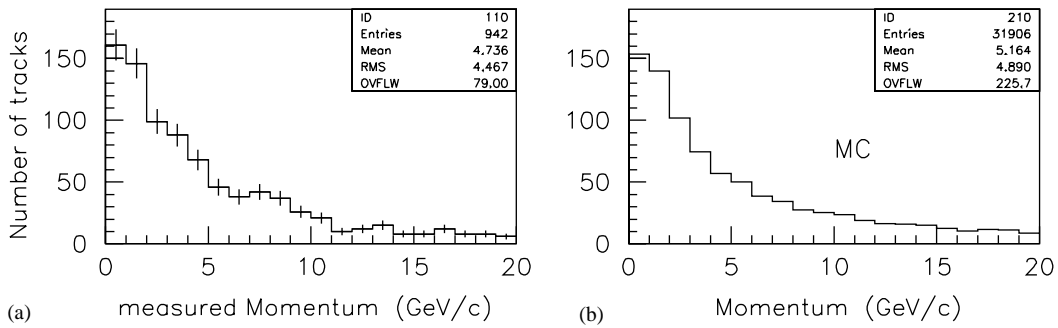
Fig. 32. Momentum distribution of the secondary particles: (a) measured by the MCS method; (b) Monte Carlo expectation. The scale of figure (b) is normalized to (a).

spectrometer measured momentum is shown in Fig. 31. The correlation is strong up to 20 GeV/c.

6.1.3. Check 3: momentum of the secondary particles

Using 942 secondary tracks from 269 located events (a subset of the 344 events), the MCS momenta were computed and the resulting distribution was compared with a Monte Carlo distribution. The results are shown in Fig. 32. The MCS momentum estimate provided a way to estimate the total event energy, which could only have been done for a few events using the magnetic spectrometer.

6.1.4. Analysis of the candidates

The momenta of the daughter tracks of the found candidates were measured by the MCS method. The resulting P_t distribution of the long-flight-decay candidates with kink topology is shown in Fig. 33. As a comparison, the expected distributions of tau decays and the hadronic secondary interactions are shown in Fig. 34.

For the short-flight-decay candidates, the measured impact parameter was investigated to see if it was consistent with the displacement due to MCS determined by the measured momentum of tracks. If the measured impact parameter was at least four times larger than the expected error, a parameter, $P_{t\,min}$, was calculated. The transverse momenta of short decays cannot be determined since the decay is only constrained to a line in space and not a point. $P_{t\,min}$ was defined as the MCS momentum of the daughter times the decay angle assuming that the decay occurs at the downstream edge of
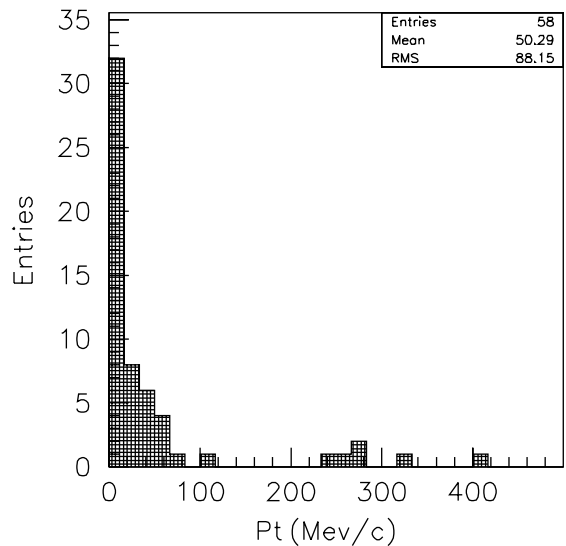

Fig. 33. P_t distribution of the detected long-flight-decay candidates.

the steel plate in which the vertex was located. (Note that the short-decay analysis applies only to ECC-type targets.) The $P_{t\,min}$ distribution of the 11 short-decay candidates is shown in Fig. 35.

6.2. Electron identification by cascade shower detection

In order to discriminate tau decays from charm decays that were associated with charged-current interactions of ν_e, ν_μ, $\overline{\nu_e}$, and $\overline{\nu_\mu}$, the existence of an electron or muon from the interaction vertex was checked.
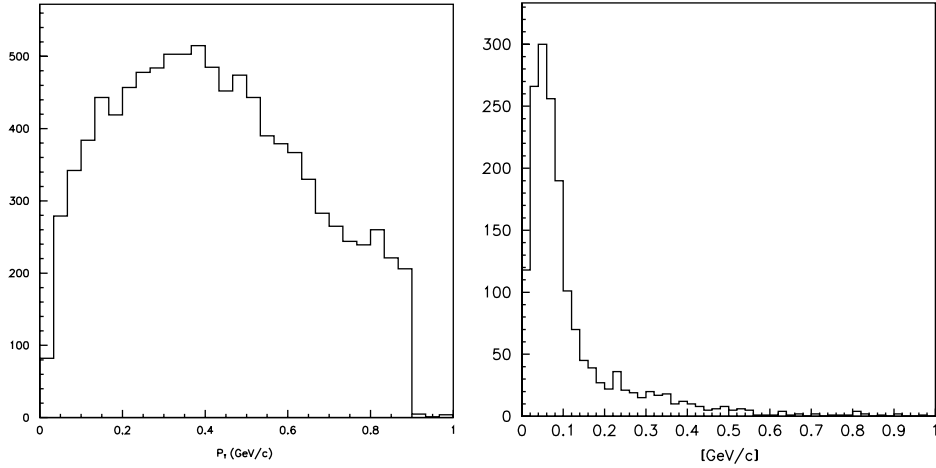
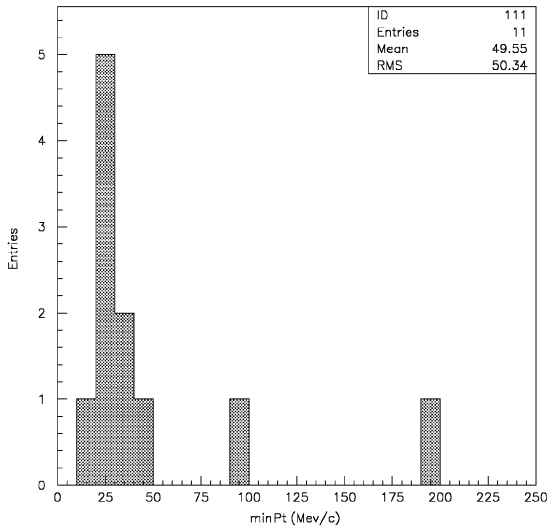Fig. 34. P_t distribution of the tau events and the secondary interactions from a Monte Carlo.

Fig. 35. $P_{t\,min}$ distribution of the detected short-flight-decay candidates.

Fig. 36. The ν_e^{CC} identification efficiency as a function of the track length.

Muons were identified conventionally with proportional tube hodoscopes downstream of steel walls. The acceptance was estimated to be 70% by a Monte Carlo. Details regarding lepton identification with the spectrometer can be found elsewhere [9]. For most events, the identification of electrons from the primary interaction was done in the emulsion targets themselves. In the emulsion, the start of an electromagnetic cascade shower was clearly identified. Another indicator is the rapid energy loss by bremsstrahlung, which appeared as
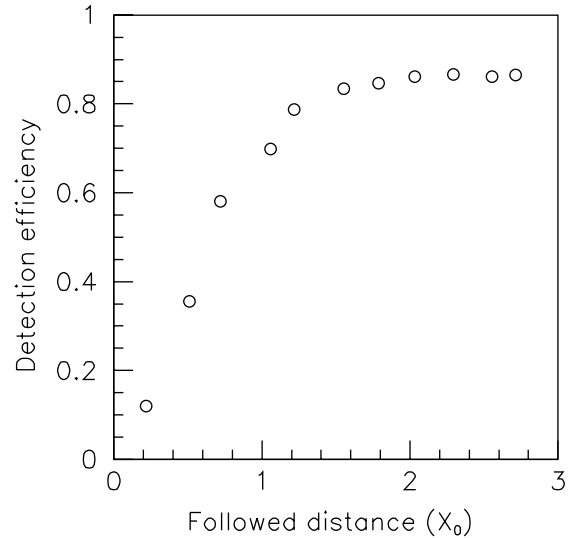
an increase of the position displacement or increase of the angle alternation by multiple Coulomb scattering as described above. The identification efficiency has a dependence on the track length followed in the emulsion. Fig. 36 shows the estimated electron identification efficiency for the electrons in the ν_e^{CC} events. Fig. 37 shows an identified event of charm production in ν_e^{CC}. Two events in the analysis sample had daughter electrons that were identified in the emulsion, and since no other electron, or muon,
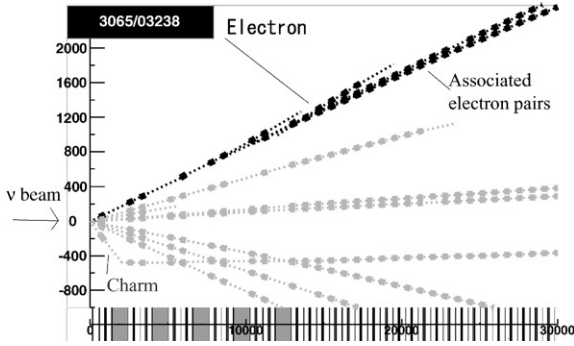
Fig. 37. Identified charm event produced in a v_e^{CC}. The upper track was identified as an electron by finding the associated electron pairs. The charm parent decayed into one track, shown in the figure near the bottom.

was found coming from the neutrino interaction, both events were identified as likely v_τ interactions.

6.3. Detection efficiency of tau decays

The detection efficiencies of τ^- from v_τ^{CC} and τ^+ from $\overline{v_\tau}^{CC}$ were estimated by Monte Carlo, which included the measured tracking efficiencies and the resolutions of the emulsion plates. Fig. 38 shows the dependence of the τ decay detection efficiency on the P_t and $P_{t\,min}$ cut for the long- and short-flight-decay search. The short-flight to long-flight ratio is significantly different between the v_τ^{CC} and $\overline{v_\tau}^{CC}$ interactions.

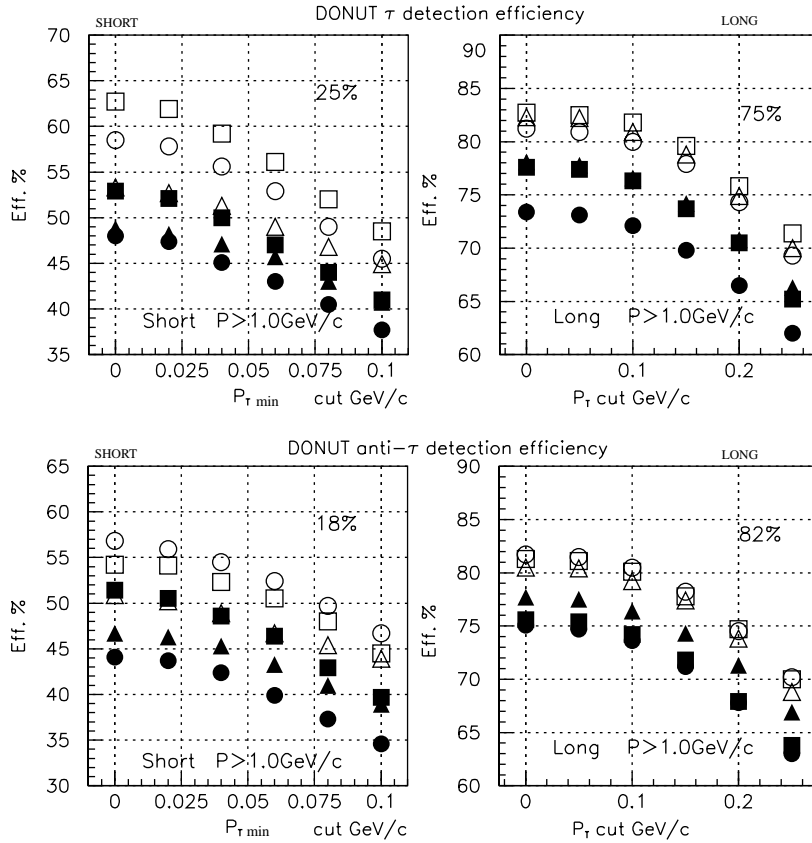
Fig. 38. Dependence of the tau decay detection efficiency on the P_t and $P_{t\,min}$ cut for the case of long and short flight decays. Top: τ^- from v_τ^{CC}. Bottom: τ^+ from $\overline{v_\tau}^{CC}$. Right: Long-flight-decay. Left: short-flight-decay. The squares, circles and triangles show the results for ECC200, ECC800 and Bulk, respectively. Open symbols indicate perfect micro-track detection efficiency and the solid symbols show the results for measured plate efficiencies.

7. Summary

The NETSCAN method of digitizing a large volume of emulsion data, devised for the DONUT analysis, was very effective for the vertex location and decay search. The NETSCAN data were also used successfully for more detailed event analysis, including momentum estimation and electron identification. The effectiveness of the NETSCAN analysis was largely due to the precise, sub-micron level of alignment achieved by careful calibration.

Those features can be considered as revival of several capabilities of the original ECC. In 1971, the discovery of X-particles (charm particles) was achieved in the analysis of the ECC exposed to cosmic rays [11]. Very precise decay search, momentum measurement by the MCS method, the identification and the energy measurements of electromagnetic showers were performed in that analysis. But it required about three months to analyze one event, because it was performed under fully human operated microscopes. In contrast with this situation, in DONUT analysis, with the help of the UTS system, about four events can be analyzed per day per UTS.

The ECC can be now be considered as a general-purpose detector. Even muon identification is possible if a number of ECC modules can be aligned along the beam. Also it is possible to determine the sign of the charged particles by installing the ECC in a magnetic field. In DONUT, the downstream counters took these last two roles.

The research and development of advanced emulsion readout systems is still in progress. With increasing scanning power, nuclear emulsion can have much wider applications in the field of elementary particle physics (especially in neutrino physics), nuclear physics and general radiation measurement.

Acknowledgements

References

[1] K. Kodama, et al., DONUT Collaboration, Phys. Lett. B 504 (2001) 218.
[2] N. Ushida, et al., E531 Collaboration, Nucl. Instr. and Meth. A 224 (1984) 50.
[3] S. Aoki, et al., CERN WA75 Collaboration, Nucl. Instr. and Meth. A 274 (1989) 64.
[4] K. Kodama, et al., Nucl. Instr. and Meth. B 93 (1994) 340;
K. Kodama, et al., Nucl. Instr. and Meth. A 289 (1990) 146.
[5] S. Aoki, et al., Nucl. Tracks 12 (1986) 249.
[6] S. Aoki, et al., Nucl. Instr. and Meth. B 51 (1990) 466.
[7] E. Eskut, et al., CHORUS Collaboration, Nucl. Instr. and Meth. A 401 (1997) 7.
[8] M. Nakamura, in: A.D. Bross, R.C. Ruchti, M.R. Wagner (Eds.), Proceedings of SCIFI93 Workshop on Scintillating Fiber Detectors, 24–28 October 1993, Notre Dame, IN, USA, World Scientific, Singapore, 1995, p. 194;
T. Nakano et al., in: A.D. Bross, R.C. Ruchti, M.R. Wagner (Eds.), Proceedings of SCIFI93 Workshop on Scintillating Fiber Detectors, 24–28 October 1993, Notre Dame, IN, USA, World Scientific, Singapore, 1995, p. 525;
T. Nakano, et al., IEEE Trans. Nucl. Sci. NS-39 (1992) 680.
[9] K. Kodama, et al., Nucl. Instr. and Meth. A submitted for publication.
[10] T. Nakano, in: Proceedings of International Workshop on Nuclear Emulsion Techniques, Nagoya, 1998.
[11] K. Niu, et al., Prog. Theor. Phys. 46 (1971) 1644.